J Mater Sci
DOI 10.1007/s10853-014-8682-5

Optimizing nano-dynamic mechanical analysis for high-resolution, elastic modulus mapping in organic-rich shales

Taylor M. Wilkinson · Saeed Zargari · Manika Prasad · Corinne E. Packard

Received: 10 July 2014 / Accepted: 24 October 2014

Abstract An elastic modulus mapping technique based on spatially continuous dynamic nanoindentation is applied to map microscale variations in a fine-grained, kerogen-rich shale consisting of inorganic minerals with an interpenetrating network of microscale pores filled with organic matter. Advantages and limitations of the application of this technique to shales are explored through varying sample preparation and scanning procedures. Filtering techniques are developed to remove data that are negatively impacted by topography and other issues inherent to the mapping technique. As a result, spatial variations of elastic modulus in kerogen-rich regions are seen at substantially higher resolution than has previously been reported. Spatial resolution and continuous mapping across high stiffness-contrast material boundaries are further improved with stringent sample preparation and the use of a sharp tip. Typical modulus values measured by this technique include approximately 10 GPa for kerogen, 15–45 GPa for clay depending on the morphology and orientation, and 50–70 GPa for quartz.

T. M. Wilkinson · C. E. Packard (✉)
Department of Metallurgical and Materials Engineering, Colorado School of Mines, Golden, CO 80401, USA
e-mail: cpackard@mines.edu

T. M. Wilkinson
e-mail: twilkins@mines.edu

S. Zargari · M. Prasad
Department of Petroleum Engineering, Colorado School of Mines, Golden, CO, USA

Introduction

Organic-rich shales are heterogeneous composite sedimentary rocks that form in sedimentary basins where abundant masses of living organisms are deposited along with silicic and carbonate minerals. The organic material, kerogen, intertwines throughout the matrix of the shale [1–3]. As the shales are buried and exposed to high temperature and pressure, the kerogen matures to produce hydrocarbons that are stored in the mature organic-rich shales as well as in adjacent formations. Economic hydrocarbon production is only feasible through high-conductivity conduits generated by the process of hydraulic fracturing.

The mechanical properties of kerogen and the physical arrangement of the material within shale reservoirs are of interest for building upscaled rock models to predict fracture propagation for hydraulic fracturing design and to interpret exploration seismic data. Mechanical properties of shales have conventionally been assessed at the cm scale and above, using uniaxial and triaxial compression tests [4], but a growing interest in determining the properties on the microscale has emerged. Serial sectioning techniques, acoustic wave technology, and computed tomography have been used to understand the arrangement of kerogen and its properties at mm to μm scales [5, 6]. Elastic modulus variations in clay minerals, shales, and natural cements have been mapped using nanoindentation, in which a diamond probe of known geometry is pressed 10–100 s of nanometers into a material while simultaneously measuring force to extract local mechanical properties [1, 7–10]. Arrays of quasistatic nanoindentations have revealed spatial variations in properties over areas of $\sim 150 \times 150$ μm [1, 11]. When these pointwise modulus maps are compared to scanning electron or optical micrographs of the same area, good correspondence is generally seen in locations of

Published online: 07 November 2014

stiff mineral components such as calcite and pyrite and softer intergranular regions; however, spatial variations below the scale of the array spacing of ~10 μm have not been resolved with this technique. Relatively large elastic and plastic zone sizes are required to reliably extract properties using the Oliver and Pharr method from these materials, and thus large spacing is required between test locations to avoid overlap [12]. Nanoindentation is capable of giving distinct mineral moduli; however, the technique often gives average or aggregate modulus values due to large indentation volumes compared to material grain size. This limitation restricts the utility of array-based nanoindentation to scales far larger than the grain sizes of most constituent particles in organic-rich shales.

Modulus mapping with finer spatial granularity is available through scanning probe methods. In this technique, a probe tip is oscillated at low displacements, typically on the order of 1 nm, while being in contact with the sample surface and is simultaneously rastered across the surface to collect data. Correspondence between the drive signal and material response is analyzed to produce a mechanical property measurement for each pixel of the scan, thus providing a spatial map of the mechanical property variation [13]. This technique has been applied to create modulus maps of biological materials and some manufactured composites [13–16], demonstrating the ability to resolve microscale mechanical property variations. From these studies, it has been seen that the use of scanning probe methods for nano-dynamic mechanical analysis (nano-DMA) enables the acquisition of modulus maps with higher spatial resolution than has previously been possible with point-based methods such as quasistatic nanoindentation.

The work presented here extends the use of scanning probe modulus mapping to Bakken shale samples collected from the Williston Basin. Modulus maps are produced over areas 5 × 5 μm in size and are compared with scanning electron micrographs of the same areas. Given the increasing use and the necessity of nano-dynamic mechanical property measurements, we discuss the effects of sample preparation, and scanning procedures are presented; both effects can negatively impact data extraction if not properly completed. While this technique allows for the collection of data at higher spatial granularity, some issues associated with the interpretation of the data become particularly pertinent when dealing with a material with high stiffness contrast, such as organic-rich shales. Both topographic variations and low signal-to-noise ratios are seen to negatively influence the ability to accurately characterize local properties within the shale. Another drawback with this technique, as well as with quasistatic indentation, is the sensitivity to the material that is below the surface of the tip and may not be visible in an image or surface scan. Modulus mapping using nano-DMA reduces the impact of subsurface interactions by reducing penetration distance to approximately 1 nm compared to quasistatic nanoindentation, which typically probes 10–100 s of nanometers into the material. As will be discussed in this paper, these issues are addressed through optimization of scanning procedures, data filtering techniques, and analysis to understand the spatial resolution of modulus maps measured on an organic-rich shale, demonstrating that this scanning probe technique can reveal property variations at significantly higher resolution than has previously been reported.

Materials and methods

The materials used in this study consist of two samples of Bakken shale recovered from the Williston Basin in North Dakota. One came from a depth of approximately 7200 ft (hereafter referred to as Shale 1). The total organic content in the core from which Shale 1 was recovered was 16 wt%. Shale 1 was sectioned, and then polished with a focused gallium ion beam (FIB)[1] using an acceleration voltage of 30 kV and beam current beginning with 30 nA and ending with 2.5 nA. The surface roughness was found to be approximately 10 nm across a 25-μm^2 area. Figure 1a shows an example SEM image taken of Shale 1 after FIB polishing. The layered texture corresponds to clay minerals, quartz and calcite are larger polygonal crystals, pyrite is white, and kerogen is black. For the most part, clays and kerogen are interspersed. A region of interest, shown in Fig. 1b, was selected for mechanical property mapping; it consisted of large regions of kerogen with small amounts of interspersed clay, a quartz grain, and several calcite grains.

The second shale came from a depth of approximately 7000 ft (Shale 2), with a total organic content of 14 wt%. Shale 2 was sectioned and then prepared using the same FIB parameters as those employed for Shale 1. However, for Shale 2, a large area was quickly and roughly polished at high beam currents to remove a substantial amount of material at once. After, Shale 2 underwent extensive milling using lower beam currents in order to decrease the surface roughness to below 2 nm across a 25-μm^2 area. Figure 2a shows a representative SEM image taken of Shale 2. The region of interest used for mechanical property mapping is shown in Fig. 2b, consisting of kerogen regions, clays mixed with kerogen, and quartz grains.

Topography and property mapping were conducted using a Hysitron TI 950 nanoindenter (Hysitron, Inc., Minneapolis, MN) equipped with nano-DMA III, a commercial nano-DMA package. Two nanoindenter tips were

[1] FEI Helios NanoLab 650, Hillsboro, OR.

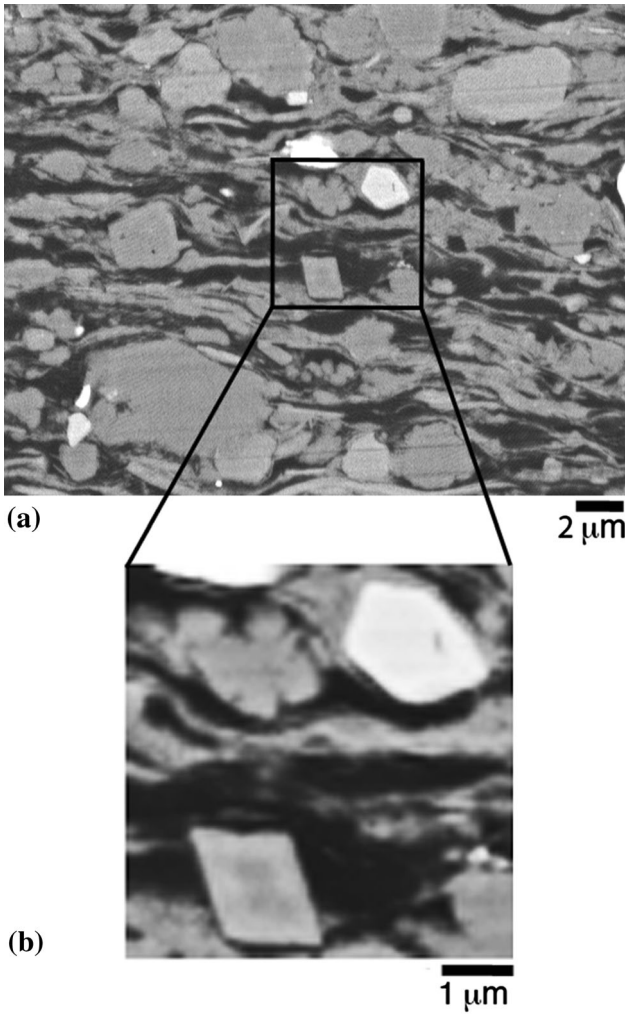

Fig. 1 **a**, **b** SEM micrograph (and corresponding enlarged region of the area of interest) of Shale 1 showing pyrite as *white*, calcite as *light gray*, and kerogen-rich regions as *black*. Data from the highlighted area are shown in Fig. 3

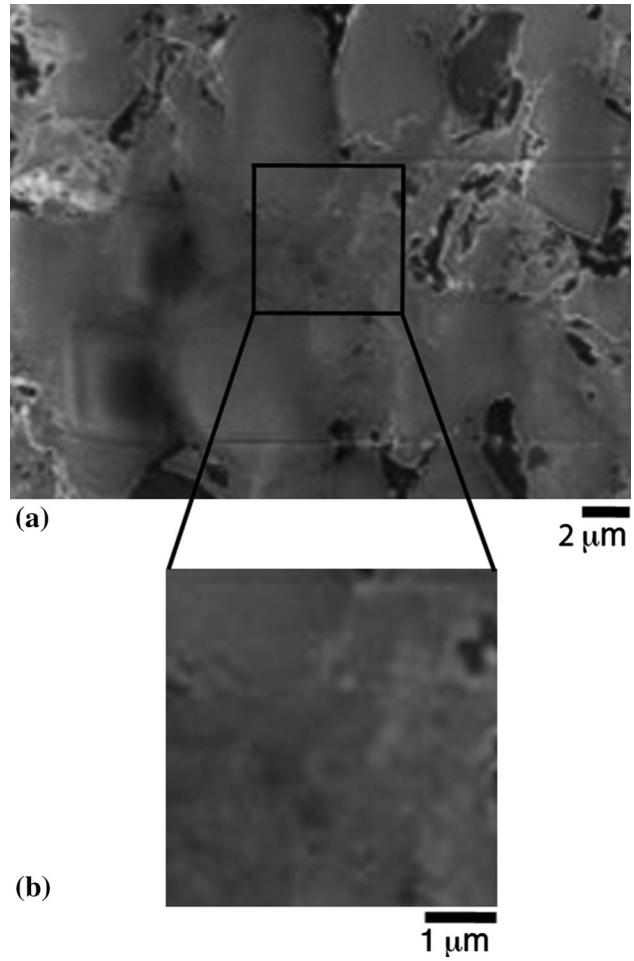

Fig. 2 **a**, **b** SEM micrograph (and corresponding enlarged region of the area of interest) of Shale 2 showing quartz as *light gray* and kerogen-rich regions as *black*. Data from the highlighted area are shown in Fig. 4

calibrated against a fused quartz sample using a quasistatic force setpoint of 2 μN to maintain contact between the tip and the sample surface, while a dynamic force of 1 μN was superimposed on the quasistatic signal at a frequency of 200 Hz. Based on a calibration-reduced modulus value of 69.6 GPa for the fused quartz, the best-fit spherical radius approximation for one tip was found to be 590 nm, while the other tip was found to be significantly sharper, at 85 nm, for the selected nano-DMA scanning parameters.

Modulus mapping was conducted using the larger radius tip on Shale 1 using a quasistatic force setpoint of 2 μN and a dynamic force of 1 μN applied at 200 Hz. Mapping of Shale 2 employed the smaller radius tip and was conducted with a quasistatic force setpoint of 2 μN and a dynamic force of 0.5 μN applied at 200 Hz. Differences in the dynamic force required to achieve similar displacement amplitudes for both samples were a consequence of tip radius. Data from regions approximately 5 × 5 μm in size were collected on both shales using a scanning frequency of 0.1 Hz. Each scan resulted in a 256 × 256 pixel data array. Elastic modulus values were calculated based on the measured stiffness at each pixel. The storage stiffness of the material, *K'*, which represents the in-phase mechanical response was calculated from the measured displacement amplitude, *X*, and phase shift, φ, according to

$$K' = \frac{F_o}{X}\cos(\varphi) + m\omega^2 - K_i, \quad (1)$$

where F_o was the applied force, ω was the oscillation frequency, *m* was the mass of the transducer, and K_i was the machine stiffness [17]. Assuming spherical contact of the indenter tip on the sample surface, the contact area over which this stiffness was distributed was calculated as a

circular area with radius equal to the contact radius, a, given as

$$a = \left(\frac{3F_oR}{2K'}\right)^{\frac{1}{2}}, \quad (2)$$

where R was the tip radius. The reduced storage modulus was then calculated as

$$E' = \frac{K'\sqrt{\pi}}{2\sqrt{A}}, \quad (3)$$

where A was the projected contact area with contact radius, a [17]. This value should not be confused with Young's modulus, though the two are related. Young's modulus represents the tensile elastic modulus measured in a linear elastic material. Under the dynamic tests, the resulting modulus is a complex modulus, which can be decomposed into storage (elastic) and loss (damping) modulus components. Furthermore, moduli acquired through indentation or dynamic modulus mapping inherently include the elastic properties of both the test material and the indenter material, and are reported as "reduced"" moduli. The reduced storage modulus is equivalent to the reduced elastic modulus for materials that do not exhibit damping [17], where the reduced elastic modulus, E_r, is defined as

$$\frac{1}{E_r} = \frac{1-v_s^2}{E_s} + \frac{1-v_i^2}{E_i}. \quad (4)$$

In Eq. (4), the subscripts of s and i correspond to the sample and indenter tip material, respectively, for the Young's modulus, E, and Poisson's ratio, ν. Reduced storage modulus is reported throughout the paper to avoid assumptions regarding the Poisson's ratios of materials encountered in the scans.

Results and analysis

Imaging samples and collecting modulus data is a straightforward process; however, it is necessary to ensure that the data are free from sample preparation and scanning procedure artifacts in order to extract reliable elastic modulus data for interpretation. In the section that follows, we present scanning results from both shale samples. The discussion begins with analysis of Shale 1, illustrating the data extraction and analysis techniques developed to remove artifacts. The results of Shale 2 are then discussed in a comparative fashion in order to show the impact of sample preparation and scanning procedure optimization on data quality and spatial resolution.

Figure 3a, which represents storage modulus data for Shale 1, shows minerals and some clay regions exhibiting moduli from 60 to 160 GPa and kerogen-rich areas taking on lower values. Figure 3b shows that Shale 1 has stiff calcite and quartz grains, which appear higher, in red, on the topography map with surrounding kerogen in green, approximately 7 nm lower. In Fig. 3, topography changes and variations in modulus are discriminated across sub-micron distances within the scans. Compared to prior studies that have utilized grids of quasistatic indentations spaced 10–14 μm apart to map similar materials [1, 11], the application of modulus mapping to this shale shows the potential of this technique to reveal property variations with substantially higher spatial resolution. However, this technique has several fundamental issues regarding the interpretation of the data that have not been addressed by previous studies, namely, (1) the influence of local surface roughness, (2) displacement amplitude variations associated with scanning a high-modulus contrast surface at fixed dynamic force, and (3) the effective spatial resolution with a scan.

The negative impact of local surface roughness on property extraction is readily observed in Fig. 3b where horizontal streaks from FIB track marks are seen. Their impact is translated into the corresponding modulus map (Fig. 3a) where ion tracks show up as property variations within relatively homogeneous materials and even across boundaries between materials in the scan. In addition, large changes in surface height occur where softer materials have been preferentially polished away compared to harder minerals (c.f. the smearing on the right side of the trapezoidal calcite grain in the bottom of Fig. 3b). These local changes in topography can lead to an over- or underestimation of contact area between the tip and the sample surface, and thus introduce errors into the property extraction when converting stiffness to modulus. For example, Fig. 3b shows that the edges of the square grain of calcite are sharp and distinct from the kerogen-rich region. The property map in Fig. 3a shows a smearing of the calcite grain properties into the kerogen regions; therefore, areas of kerogen are sometimes negatively influenced by neighboring materials.

To reduce the impact of topographic variations on the interpretation of modulus maps, a filtering scheme is implemented. First, we consider the contact radius of the 590-nm tip with the sample under a quasistatic setpoint load of 2 μN to understand the extent of the area probed by the tip. In this calculation, the sample is assumed to have a completely flat surface so that there is a uniform contact area for the tip to probe the surface of the material. Based on reported values of elastic moduli of the materials identified within the sample, ranging from 10 GPa for kerogen to 306 GPa for pyrite [1, 3, 18], the contact radius varies from 11 to 35 nm for the stiffest and the most compliant materials, respectively. Comparison of these

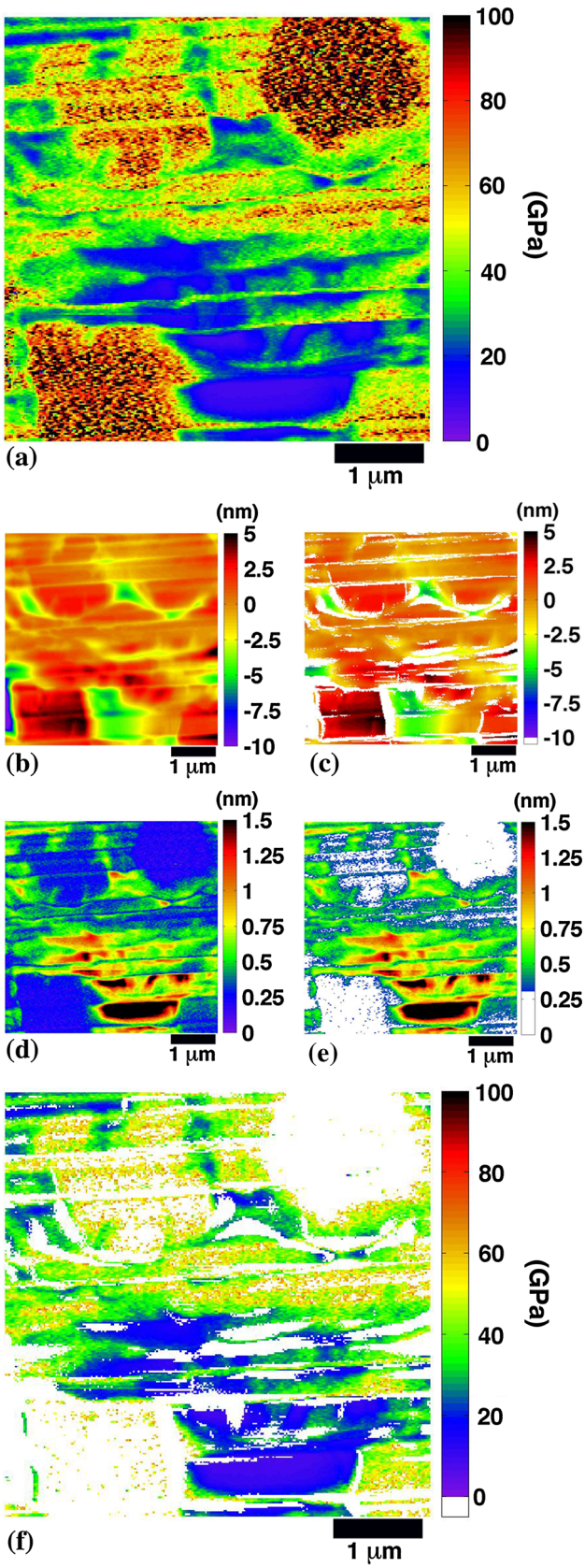

◀**Fig. 3** **a** Modulus map collected for Shale 1 from the region highlighted in Fig. 1. **b**, **c** Raw topographic scan and corresponding filtered (0.3 nm) topography scan. **d**, **e** Raw displacement amplitude scan and corresponding filtered (0.3 nm) displacement amplitude scan. **f** A filtered modulus map of Shale 1 based on topographic and displacement amplitude filters (Color figure online)

bounding contact radii to the map pixel size of 19.5 × 19.5 nm for a 5 by 5 μm scan illustrates that material from the nearest neighbor pixels within a scan influence the data gathered at each location for the compliant materials; therefore, a filter is implemented that evaluates the surface height difference between nearest neighbor pixels throughout the Shale 1 topography scan and masks data from pixels that exhibit a height difference of greater than 0.3 nm. This cut-off is empirically acquired and results in removal of the most areas affected by ion track marks and other sharp topographic variations for the region studied here, making up approximately 20 % of the scan. A filtered topographic scan can be viewed in Fig. 3c, where data are removed around the square calcite piece in the lower left-hand corner of the image due to the large height difference that was created between the stiff calcite and the compliant kerogen during sample preparation. The ion track marks seen horizontally across Fig. 3b, in yellow, have also been removed. Regions where data have been removed would result in erroneous local contact area estimations and bias the storage modulus values reported in Fig. 3a.

A second issue apparent in Fig. 3a is questionable modulus values on several of the mineral components. Note, in Fig. 3a, the circular piece of pyrite in the upper left-hand corner of the image shows modulus values of approximately 80 GPa; however, the reported values for pyrite are upwards of 300 GPa [18]. Closer examination of the raw data used to produce the modulus map reveals that displacement amplitude in the stiff mineral regions overwhelmingly falls below 0.3 nm (see Fig. 3d). Displacement amplitudes below 0.3 nm are not sufficiently above the noise floor of the instrument [19]; thus, it is unsurprising that quantitative values for modulus in the affected regions are erroneous. In regions where displacement amplitude is below 0.3 nm, error is magnified due to insufficient material strain in high modulus materials for the given test force. Displacement amplitudes in the kerogen-rich regions of the scan are 1–1.7 nm for the same scanning parameters. These higher displacement amplitude values are sufficiently above the noise floor and simultaneously low enough that plastic deformation is avoided, so property extraction from more compliant regions is less likely to be negatively impacted at low dynamic forces.

Increasing the dynamic load can result in higher displacement amplitude to make property measurements on mineral phases; however, this approach would risk the fidelity of the measurements conducted in low-modulus regions by causing plastic deformation or nonlinear elastic deformation. Filtering is performed on the scan to mask any pixels with inadequate displacement amplitude to ensure that only data with sufficiently high signal-to-noise ratio are examined. Figure 3e shows that the large calcite grain (lower left-hand corner) and the piece of pyrite (upper right hand corner) have been removed due to low displacement amplitudes. Kerogen-rich regions remain intact throughout the image of Fig. 3e; however, final analysis shows approximately 30 % of the scan was removed during filtering.

Once each filtering technique was completed, scans from Fig. 3c, e were used to filter affected data from the modulus map in Fig. 3a. If a pixel was filtered due to either too much neighboring surface height variation or an insufficient displacement amplitude, then the data from that pixel location were removed from Fig. 3a and replaced with a white pixel. The resulting filtered modulus map is located in Fig. 3f, where the effects of filtering can be seen in comparison to Fig. 3a with ion track marks and several of the stiff minerals are masked, while parts of two calcite grains and large, kerogen-rich areas are left behind. Shale 1 has intermixed clay and exhibits lower moduli values in the range of 20–50 GPa through the scan in Fig. 3f.

Though modulus mapping provides data at extremely high granularity, especially compared to quasistatic indentation arrays, it is relevant to consider the effective spatial resolution of the scans to identify the extent to which the properties indicated in a pixel are influenced by the surrounding volume of material. The modulus mapping technique used in this study uses fixed set-point and dynamic loads through an entire scan; however, the contact radius varies at each point based on the stiffness of the specific location under test within the inhomogeneous sample. Assuming Hertzian contact and isotropic elasticity under the contact, one can estimate the volume that is probed at each pixel location as a roughly hemispherical volume of radius equal to three times the contact radius. Areas located at distances greater than 3a (where a is the contact radius defined in Eq. 1) from the center of contact contribute little, as the stresses drop to less than 10 % of their maximum values [20]. This information is used to estimate the effective lateral spatial resolution in the scan as between 66 and 210 nm, where the lower bound corresponds to stiff mineral areas with a modulus of 306 GPa and the upper bound corresponds to compliant, organic-rich areas with a modulus of 10 GPa. Given the scan size examined here, this spatial resolution corresponds to 3–10 pixels. Although the tip displaces into the surface by only ~ 1 nm, material within a zone extending 33–105 nm below the surface impacts local property measurements. This submicrometer resolution in determining elastic properties in an organic-rich shale, though not as fine as the granularity of data collected in the scans, represents significantly finer scale resolution than is acquired by pointwise quasistatic nanoindentation, which probes volumes with radii of hundreds to thousands of nanometers for indentation depths typically used for property measurement.

While Shale 1, and its subsequent analysis, has given insight into the nanoscale interactions of these stiff and compliant materials, a large amount of the data, almost 40 % in total, were lost due to filtering. These filtering techniques removed data due to large surface height variations as well as low displacement amplitudes. Both issues would result in an inaccurate calculation of properties. In an attempt to improve data retention, changes were made to the sample preparation and scanning procedures for imaging Shale 2. An analysis of the data collected for Shale 2 is presented below.

Figure 4a, b shows a modulus map and corresponding topographic scan, respectively, of the region of interest for Shale 2. When Fig. 2b is used in conjunction with Fig. 4a, the storage modulus values for the given areas in the SEM show that quartz regions (yellow/orange/red regions) range from 50 to 80 GPa, while the kerogen-rich regions are located in blue region and exhibit moduli between 10 and 20 GPa. The green regions seen throughout the scan are the mixed clay and kerogen regions, which correspond to moduli values between 30 and 45 GPa. These more uniform property values partially result from the improved surface condition, as seen in the topography map in Fig. 4b. While topography varied approximately 10 nm over a 25-μm^2 area for Shale 1 (Fig. 3b), this was reduced greatly to approximately 2 nm over an equivalent 25-μm^2 area for Shale 2 (Fig. 4b). This reduction in surface topography is a result of more stringent sample preparation as presented in the Methods section. The stiffer minerals in Shale 2, such as quartz, can be seen in Fig. 4b as dark orange, and they are located throughout the scan, surrounded by a mixture of kerogen-rich regions (yellow regions in Fig. 4b) as well as areas of clays mixed with kerogen (light orange regions in Fig. 4b). Unlike Shale 1, the topography was much more uniform for Shale 2. It is also important to note that the improved ion milling removed the majority of the issues of track marks seen in Shale 1.

The same topography filtering technique used for Shale 1 was used to analyze Shale 2 to determine whether or not improved surface preparation could reduce the amount of filtered data, resulting in a more complete modulus map. Figure 4c shows the corresponding filtered topographic image for Shale 2. A surface height variation of 0.3 nm

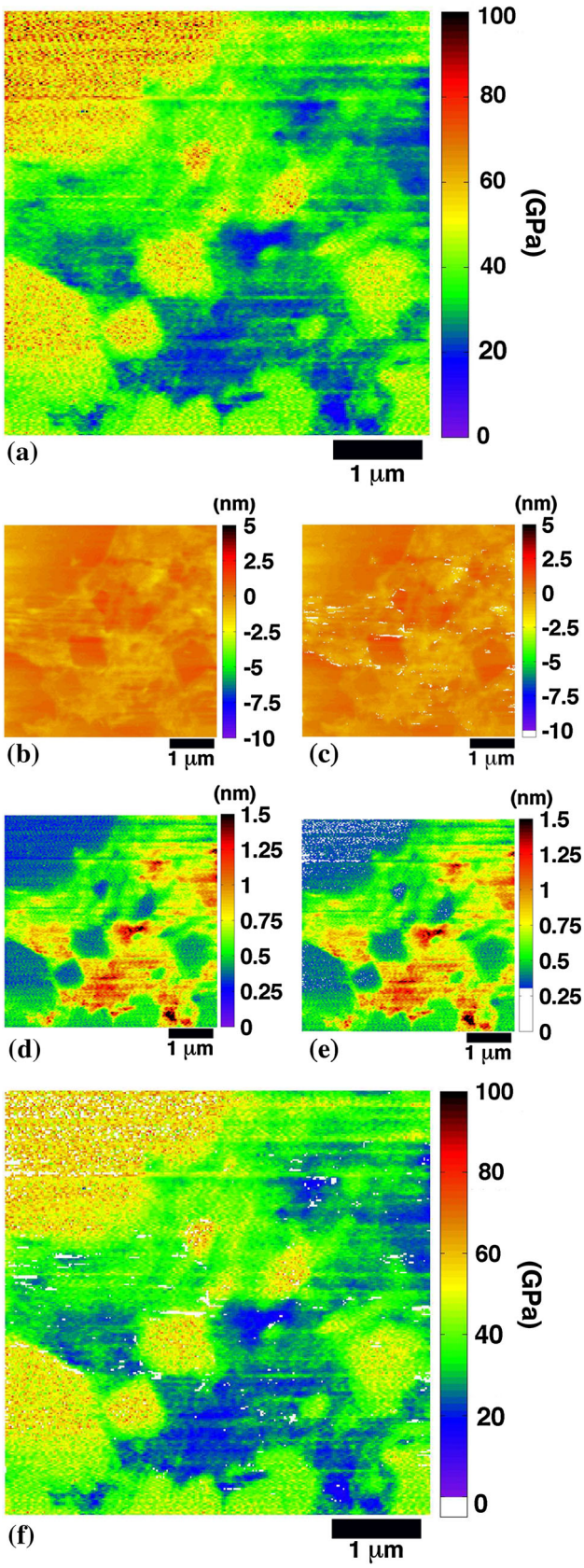

◀**Fig. 4** **a** Modulus map collected for Shale 2 for the region highlighted in Fig. 2. **b**, **c** Raw topographic scan and corresponding filtered (0.3 nm) topography scan. **d**, **e** Raw displacement amplitude scan and corresponding filtered (0.3 nm) displacement amplitude scan. **f** A filtered modulus map of Shale 2 based on topographic and displacement amplitude filters (Color figure online)

was used again to analyze the scan. Previously, the filtering technique removed close to 20 % of the scan of Shale 1. Figure 4c shows less than 5 % of the entire scan is removed due to surface height variations. When the calculations for the amount of material probed were conducted, it was found that the contact radius varied from 5 to 15 nm. For a 5 × 5 μm scan, these numbers correspond to less than 1 pixel for both compliant and stiff areas of the scan. Thus, it is still sufficient to consider topographic variations only between nearest neighbor pixels. In fact, the use of the topography filter for Shale 2 may be overly conservative; even with drastic filtering, Fig. 3c remains largely intact. This is due to the dramatically sharper tip as well as the lower dynamic load being used. Reducing the dynamic load using the larger radius tip used for Shale 1 would not yield similar results, but instead would result in the majority of the scan falling below the noise floor of the machine due to insufficient strain.

Once topography filtering was completed, the displacement amplitude scan for Shale 2 was analyzed. Similar to Shale 1, displacement amplitude data that fell below 0.3 nm in Shale 2 were masked and removed from the final analysis of the shale. Previously, approximately 30 % of the scan of Shale 1 (Fig. 3e) was removed due to the displacement amplitude being below the noise floor of the machine. Figure 4e has less than 5 % of the scan removed due to displacement amplitude values below 0.3 nm. Again, the regions where data were removed fell within the stiffer mineral components. This can be seen in the upper left-hand corner of Fig. 4e where data were removed from the quartz grain. Shale 2 scanning parameters were optimized for kerogen-rich regions, just as was done for Shale 1; however, with better sample preparation and a sharper tip, more data remained after filtering techniques were implemented.

These filtering techniques in combination resulted in the filtered storage modulus map in Fig. 4f. Less than 5 % of the collected data were removed from the scan due to topographic variations or inadequate displacement amplitude values. Figure 4f is a drastic improvement over the 40 % of data that were removed during the analysis of Shale 1 (Fig. 3f). Note that the areas of transition from compliant to stiff material are sharp, denoting a change in properties. For example, in the lower left-hand corner of

the image, the circular mineral piece is surrounded by pore-filling mineral deposits (in green corresponding to ~40 GPa) and finally by softer mineral regions (in blue corresponding to ~15 GPa). The effective spatial resolution for Shale 2 varied between 30 and 90 nm, which corresponded to a spatial resolution of 2 to 5 pixels. This is another improvement over the resolution seen for Shale 1, which varied from 3 to 10 pixels. The analysis of Shale 2 found that a sharper tip and more stringent surface preparation resulted in the ability to collect data with a consistent uniform contact area as well as data above the noise floor of the machine. This ultimately led to a more intact final scan once the analysis and filtering techniques had been applied to the highly heterogeneous shale.

While Shale 1 offers some useful insight, a large portion of the scan is removed due to large topography variations and a lack of displacement amplitude; Shale 2 provides a largely intact scan, which allows for simultaneous analysis of both compliant and stiff regions. In both scans, the data show submicron spatial variations in reduced storage modulus; however, with adequate sample preparation and a sharp tip, the amount of data that can be maintained for analysis of local modulus variations after filtering is greatly increased.

Conclusion

Two Bakken shale samples were characterized using a nanoindentation-based dynamic modulus mapping technique. The shales exhibited large stiffness contrasts that can jeopardize accurate data collection if proper preparation of a smooth surface is not ensured. We find here that a surface roughness of 2 nm is adequate for obtaining high-resolution scans, but that roughness values of 10 nm or larger result in an unacceptable amount of negatively impacted data. Implementing a filter that removes data where neighboring pixels differ by a height of more than 0.3 nm avoids locally inaccurate contact radius assumptions due to topographic variation and resulting inaccurate elastic modulus values. The large stiffness contrasts of shale constituent materials also make it difficult to achieve reasonable displacement amplitude values that are both above the noise floor of the machine and do not result in plastic deformation of the sample, unless a sufficiently sharp tip and optimized dynamic force are utilized. Elastic modulus values acquired from regions where displacement amplitude falls below 0.3 nm reflect inaccurate data as a result of insufficient strain in the locally probed area. Filtering techniques were applied to mask areas negatively impacted by high roughness or low displacement amplitude, resulting in property maps that are more quantitatively accurate in interpreting local property variation. While this approach provides submicrometer spatial resolution in mapping modulus variations within microscale kerogen-rich regions, which are too small to be accurately probed by quasistatic nanoindentation, nanodynamic modulus mapping techniques can be optimized by ensuring the highest quality FIB preparation and employing a sufficiently sharp tip to maintain more of the collected data. It was found that Shale 1 lost approximately 40 % of its data due to filtering, while Shale 2 lost less than 5 %. Typical modulus values measured by this technique include approximately 10 GPa for kerogen, 15–45 GPa for clay depending on the morphology and orientation, and 50–70 GPa for quartz. This improvement in data extraction provides a better understanding of intergranular properties in shales and is applicable to other natural and manufactured composites containing stiff and compliant materials. The data presented here for organic-rich shales are the first of their kind and have the potential to inform procedures for upscaling to representative volume elements and developing physics-based models for assessing deformation and fracture potential.

Acknowledgements The data for this paper are available at the Colorado School of Mines data repository. The authors thank the OCLASSH consortium based at the Colorado School of Mines for the samples and their support, and Lyn Canter for sample preparation and valuable discussions. Taylor Wilkinson also acknowledges the financial support provided by the Abernathy Fellowship.

References

1. Ahmadov R, Vanorio T, Mavko G (2009) Confocal laser scanning and atomic-force microscopy in estimation of elastic properties of the organic-rich Bazhenov Formation. Rock Phys 1:18–23. doi:10.1190/1.3064141
2. Bobko C, Ulm F-J (2008) The nano-mechanical morphology of shale. Mech Mater 40:318–337. doi:10.1016/j.mechmat.2007.09.006
3. Zeszotarski JC, Chromik RR, Vinci RP, Messmer MC, Michels R, Larsen JW (2004) Imaging and mechanical property measurements of kerogen via nanoindentation. Geochim Cosmochim Acta 68:4113–4119. doi:10.1016/j.gca.2003.11.031
4. Vernik L, Nur A (1992) Ultrasonic velocity and anisotropy of hydrocarbon source rocks. Geophysics 57:727–735
5. Prasad M, Mba K, Sadler T, Batzle M (2011) Maturity and impedance analysis of organic-rich shales. SPE Reservoir Eval Eng 14:533–543. doi:10.2118/123531-PA
6. Vega B, Dutta A, Kovscek AR (2014) CT imaging of low-permeability, dual-porosity systems using high x-ray contrast gas. Transport Porous Med 101:81–97. doi:10.1007/s11242-013-0232-0
7. Kopycinska-Müller M, Prasad M, Rabe U, Arnold W (2007) Acoust ImagSpringer
8. Prasad M, Kopycinska M, Rabe U, Arnold W (2002) Measurement of Young's modulus of clay minerals using atomic force acoustic microscopy. Geophys Res Lett 29:13-1–13-4. doi:10.1029/2001GL014054
9. Ulm F-J, Abousleiman Y (2006) The nanogranular nature of shale. Acta Geotech 1:77–88. doi:10.1007/s11440-006-0009-5
10. Zargari S, Prasad M, Mba KC, Mattson ED (2013) Organic maturity, elastic properties, and textural characteristics of self resourcing reservoirs. Geophysics 78:D223–D235. doi:10.1190/geo2012-0431.1

11. Zhu W, Hughes JJ, Bicanic N, Pearce CJ (2007) Nanoindentation mapping of mechanical properties of cement paste and natural rocks. Mater Charact 58:1189–1198. doi:10.1016/j.matchar.2007.05.018
12. Constantinides G, Ravi Chandran K, Ulm F-J, Van Vliet K (2006) Grid indentation analysis of composite microstructure and mechanics: principles and validation. Mater Sci Eng A-Struct 430:189–202. doi:10.1016/j.msea.2006.05.125
13. Balooch G, Marshall GW, Marshall SJ, Warren OL, Asif SA, Balooch M (2004) Evaluation of a new modulus mapping technique to investigate microstructural features of human teeth. J Biomech 37:1223–1232. doi:10.1016/j.jbiomech.2003.12.012
14. Gaboriaud F, Dufrêne YF (2007) Atomic force microscopy of microbial cells: application to nanomechanical properties, surface forces and molecular recognition forces. Colloid Surface B 54:10–19. doi:10.1016/j.colsurfb.2006.09.014
15. Ryou H, Pashley DH, Tay FR, Arola D (2013) A characterization of the mechanical behavior of resin-infiltrated dentin using nanoscopic dynamic mechanical analysis. Dent Mater 29:719–728. doi:10.1016/j.dental.2013.03.022
16. Sahin O, Erina N (2008) High-resolution and large dynamic range nanomechanical mapping in tapping-mode atomic force microscopy. Nanotechnology 19:445717. doi:10.1088/0957-4484/19/44/445717
17. Syed Asif SA, Wahl KJ, Colton RJ, Warren OL (2001) Quantitative imaging of nanoscale mechanical properties using hybrid nanoindentation and force modulation. J Appl Phys 90:1192. doi:10.1063/1.1380218
18. Mavko G, Mukerji T, Dvorkin J (2009) The rock physics handbook: tools for seismic analysis of porous media. Cambridge University Press, Cambridge
19. Hysitron (2012) TI 950 TriboIndenter User Manual
20. Fischer-Cripps AC (2007) Introduction to contact mechanics. Springer, New York